Geophysical Research Letters

RESEARCH LETTER

10.1029/2020GL087929

Forcing Dependence of Atmospheric Lapse Rate Changes Dominates Residual Polar Warming in Solar Radiation Management Climate Scenarios

Matthew Henry[1] and **Timothy M. Merlis**[2]

[1]Department of Mathematics, University of Exeter, Exeter, UK, [2]Department of Atmospheric and Oceanic Sciences, McGill University, Montreal, Quebec, Canada

Key Points:

- Idealized GCM simulations show residual polar warming when the solar constant is reduced to compensate for an increase in greenhouse gases
- A single column model is used to decompose the high-latitude temperature change into the effects of the changes in CO_2, insolation, and energy transport change
- This decomposition shows the importance of the enhanced near-surface warming from the CO_2 increase in explaining the residual polar warming

Supporting Information:

- Supporting Information S1

Correspondence to:
M. Henry,
m.henry@exeter.ac.uk

Citation:
Henry, M., & Merlis, T. M. (2020). Forcing dependence of atmospheric lapse rate changes dominates residual polar warming in solar radiation management climate scenarios. *Geophysical Research Letters*, *47*, e2020GL087929. https://doi.org/10.1029/2020GL087929

Received 18 MAR 2020
Accepted 17 JUL 2020
Accepted article online 19 JUL 2020

Abstract Simulations of solar radiation management (SRM) geoengineering using comprehensive general circulation models show a residual surface warming at high latitudes. Previous work attributes this to the difference in forcing structure between the increase in greenhouse gases and decrease in insolation, but this neglects the role of the induced reduction in atmospheric energy transport. Here we show that the difference in vertical structure of temperature change between increasing CO_2, decreasing insolation, and decreasing atmospheric energy transport is the dominant reason for the residual near-surface warming at high latitudes. A single-column model (SCM) is used to decompose the high-latitude temperature change and shows the importance of the enhanced near-surface warming from the CO_2 increase in explaining the residual polar warming. This suite of models invites caution when attributing high-latitude surface temperature changes to the lapse rate feedback, as various forcings and nonlocal processes affect the vertical structure of temperature change differently.

Plain Language Summary Solar radiation management (SRM) geoengineering has been proposed as a way of counteracting the warming effects of increasing greenhouse gases by reflecting solar radiation. When the carbon dioxide concentration (CO_2) is quadrupled and the solar constant is reduced in climate models to reach zero global mean surface temperature change, there is still residual warming in polar regions. Previous analyses suggested that it was caused by the latitudinal difference in forcing between the CO_2 increase and insolation reduction. This work shows the importance of the differences in vertical structure of atmospheric temperature change between the CO_2 increase and solar radiation reduction in explaining this residual polar warming. This underlines the importance of considering the vertical structure of temperature change caused by a given forcing when trying to understand what shapes the pattern of surface temperature change.

1. Introduction

Proposed solar radiation management (SRM) geoengineering schemes aim to counteract the radiative forcing and warming from anthropogenic emissions. One widely discussed method of SRM is to inject sulfate aerosols or their precursors in the stratosphere. Simulations of aerosol injection produce similar surface and tropospheric temperature changes to simulations that simply reduce the solar constant, although the stratosphere and the partitioning between direct and diffuse solar radiation reaching the surface differ between the two experiments (Kalidindi et al., 2015). The experiment G1 of the Geoengineering Model Intercomparison Project (GEOMIP) consists of reducing the solar constant to compensate for abruptly quadrupled CO_2 concentrations in fully coupled general circulation models (GCMs) (Kravitz et al., 2011). The temperature difference between the preindustrial and G1 experiments shows a residual polar warming: The surface air temperature change is positive near the poles and slightly negative in the tropics (Stocker et al., 2013).

Figures 1a and 1c show the atmospheric and surface temperature change, respectively, between the geoengineered G1 experiment and preindustrial control climate from five comprehensive climate models (listed in the legend of Figure 1c). While there is a slight surface cooling in the tropics, the high latitudes of both hemispheres have from 0.5 K to 2 K of residual warming. This residual polar warming has important consequences for the shift in the intertropical convergence zone (ITCZ) and changes in atmospheric energy transport in solar geoengineered climates (Russotto & Ackerman, 2018). It is also relevant to our

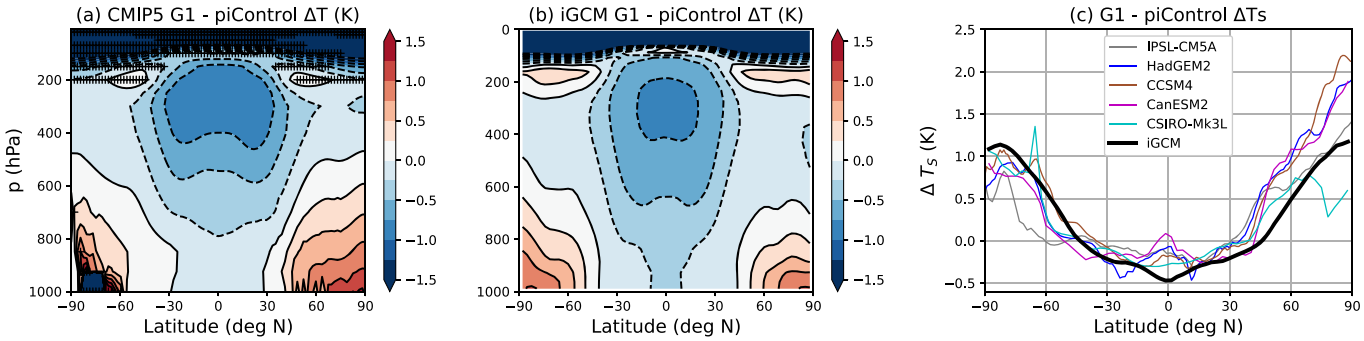

Figure 1. Residual polar warming occurs in climate model simulations of solar radiation management geoengineering. Temperature change between the solar geoengineered simulation (G1) and the preindustrial control simulation (piControl) from (a) mean of five CMIP5 models (IPSL CM5A, HadGEM2, CCSM4, CanESM2, and CSIRO-Mk3L) and (b) idealized GCM. Crosses in panel (a) indicate regions where the intermodel standard deviation is larger than 1.5. (c) Surface temperature changes from the five CMIP5 models (colors) and the idealized GCM (black).

understanding of the polar amplification of surface temperature change and vertical structure of temperature change under increased CO_2 (Henry & Merlis, 2019; Manabe & Wetherald, 1975; Pithan & Mauritsen, 2014).

This residual polar warming is commonly explained by the difference in latitudinal forcing structure between the increase in greenhouse gases and the decrease in insolation, which leads to a positive top-of-atmosphere (TOA) forcing at the poles, a negative TOA forcing in the tropics, and a near-zero global-mean TOA forcing (Govindasamy & Caldeira, 2000). The tropically amplified CO_2 forcing results from the climatological atmospheric lapse rate being larger in the tropics than near the poles (Huang et al., 2016), although it is more latitudinally homogeneous than the forcing from reduced insolation (Hansen et al., 1997). This explanation, however, does not account for changes in atmospheric energy transport that result from latitudinally inhomogeneous TOA forcing. In Merlis and Henry (2018), we compute an analytic estimate of the effect of the different latitudinal structure of the solar and CO_2 forcings on the surface air temperature change in geoengineered climates that includes the effect of energy transport: We find that this effect accounts for approximately half of the total residual polar warming in the absence of regional climate feedback mechanisms.

The vertical structure of atmospheric temperature change is enhanced in the upper troposphere in the tropics and enhanced near the surface in high latitudes (Figure 1a). We will use "top-heavy" and "bottom-heavy" to mean enhanced in the upper troposphere and near the surface, respectively. In the tropics, the atmosphere is close to radiative-convective equilibrium: Radiative cooling is balanced by convective heating. The vertical structure of temperature is approximately determined by the moist adiabat; hence, the lapse rate is uniquely a function of surface temperature and relative humidity. Therefore, the lapse rate change depends only on the surface temperature change, assuming no change in relative humidity (Xu & Emanuel, 1989). Near the poles, however, the atmosphere is close to "radiative-advective" equilibrium: Warming from atmospheric energy transport is balanced by radiative cooling. Cronin and Jansen (2016) use an analytic radiative-advective model of the high-latitude atmosphere to show that the lapse rate response differs depending on the nature of the forcing. In their model, a positive surface forcing (e.g., an increase in convergence of ocean heat transport or absorbed solar radiation at the surface) induces a destabilizing lapse rate change, a positive longwave radiative forcing induces a more destabilizing lapse rate change than the surface forcing, and an increase in atmospheric energy transport and/or solar atmospheric heating induces a weakly stabilizing or neutral lapse rate change. Moreover, they suggested that each additional feedback such as water vapor, clouds, or surface albedo would induce a different lapse rate response. This simple model led to the important insight that the high-latitude lapse rate change is forcing dependent. However, a change in atmospheric energy transport leads to a vertically uniform temperature change because of the simplified representation of the energy transport's vertical structure in the analytic radiative-advective model. Atmospheric energy transport convergence has been suggested to preferentially affect the middle troposphere in high latitudes in comprehensive climate models (Laliberté & Kushner, 2013).

In this paper, we compare idealized and comprehensive GCM simulations of SRM. We quantify the contributions of forcings and feedbacks to the total high-latitude lapse rate change and concomitant surface temperature change using a single-column model (SCM). The central result is that the CO_2 forcing has a temperature response that is more surface-enhanced than the reductions in solar forcing and atmospheric energy transport, leading to a relatively large surface temperature response for the small total forcing.

2. Idealized GCM Experiment

We implement an SRM experiment using an idealized atmospheric GCM. A version of the Geophysical Fluid Dynamics Laboratory (GFDL) atmospheric GCM is used with no clouds, comprehensive clear-sky radiation, annual-mean insolation, and aquaplanet surface boundary conditions with no sea ice. This setup is similar to Merlis et al. (2013) and to the Model of an Idealized Moist Atmosphere (MiMA) (Jucker & Gerber, 2017). In order to compensate for the cooling radiative effect of clouds, the surface albedo is set to be an approximation of Earth's TOA albedo (Figure S1 in the supporting information) instead of prescribing an idealized cloud distribution (Merlis et al., 2013) or uniformly increasing the surface albedo (Jucker & Gerber, 2017). The control simulation has a CO_2 concentration of 300 ppm, and the solar constant is 1,365 W m^{-2}. The solar constant in the SRM run is decreased to 1,317 W m^{-2} (a 3.5% reduction) in order to get zero-mean surface air temperature change when the CO_2 concentration is quadrupled. Figure S2a shows the atmospheric temperature for the control simulation, and it compares well with Earth's climate.

The surface boundary condition of the idealized atmospheric GCM is an aquaplanet with a slab mixed layer ocean with the heat capacity of 1 m of water and no representation of ocean heat transport. The GCM's spectral dynamical core has T42 spectral truncation for a nominal horizontal resolution of $2.8° \times 2.8°$ and 30 vertical levels. The skin temperature is interactively computed using the surface radiative and turbulent fluxes, which are determined by bulk aerodynamic formulae. A k-profile scheme with a dynamically determined boundary layer height is used to parametrize the boundary layer turbulence. The GCM uses a simplified Betts-Miller convection scheme (Frierson, 2007). The large-scale condensation is parameterized such that the relative humidity does not exceed one and the condensed water is assumed to immediately return to the surface. The model uses the comprehensive radiation scheme described in Anderson et al. (2004) with annual mean insolation and a solar constant equal to 1,365 W m^{-2}. The surface has no representation of sea ice other than the surface albedo distribution; hence, there is no surface albedo feedback. All simulations are run for 6,000 days with time averages over the last 3,000 days shown, when all climate states have reached a statistical steady state.

We perform four simulations. The control simulation has 300 ppm of CO_2 and a 1,365 W m^{-2} solar constant. The increased CO_2 simulation has 1,200 ppm of CO_2. The reduced solar constant experiment has a 1,317 W m^{-2} solar constant. The SRM experiment has both increased CO_2 and a reduced solar constant. The value for the reduced solar constant was determined in order to get near-zero global surface air temperature change. Figure S2b shows the temperature difference between the control and increased CO_2 simulation, and Figure S2c shows the temperature difference between the control and decreased solar constant simulation.

Figure 1b shows the atmospheric temperature change between the control and SRM idealized GCM simulations, which has a similar structure to that of comprehensive GCMs (Figure 1a). The surface temperature change between the control and SRM run in the idealized GCM (black) is also reasonably close to the comprehensive GCMs (Figure 1c). In addition, the change in atmospheric energy transport is similar to that of comprehensive GCMs (a reduction of 0.1 PW in midlatitudes; Figures S3b and 1 of Russotto & Ackerman, 2018). This model's ability to reproduce the temperature and atmospheric energy transport changes from comprehensive GCM simulations suggest that processes present in this idealized model are sufficient to explain the ensemble-mean changes in SRM experiments. The idealized GCM underestimates the surface temperature change from comprehensive GCMs in the northern extratropics while slightly overestimating warming in the southern extratropics. This may be due to the absence of the surface albedo feedback (which enhances Northern Hemisphere warming) and ocean heat uptake (which moderates Southern Hemisphere warming) in the idealized GCM. We proceed to decompose the high-latitude temperature response in this GCM to identify the mechanism responsible for residual polar warming.

3. SCM Experiments

To decompose the high-latitude temperature change in the idealized GCM simulation, we use the SCM from the ClimLab python package for process-oriented climate modeling (Rose, 2018) to emulate the high-latitude troposphere of the idealized GCM. The temperature tendency budgets for atmospheric and surface temperature are given by the following equations:

$$\frac{\partial T_a(p)}{\partial t} = \left.\frac{\partial T_a(p)}{\partial t}\right|_{\text{rad}} + \left.\frac{\partial T_a(p)}{\partial t}\right|_{\text{adv}} + \left.\frac{\partial T_a(p)}{\partial t}\right|_{\text{cond}}, \tag{1}$$

$$\frac{\partial T_s}{\partial t} = \left.\frac{\partial T_s}{\partial t}\right|_{\text{rad}} + \left.\frac{\partial T_s}{\partial t}\right|_{\text{SH}} + \left.\frac{\partial T_s}{\partial t}\right|_{\text{LH}}, \tag{2}$$

where t is time and p is pressure (with 40 pressure levels). The subscripts "rad", "conv", "adv", "cond", "SH", and "LH" refer to radiative, convective, advective, condensation, sensible heat flux, and latent heat flux temperature tendencies, respectively. The radiative, convective, sensible heat flux, and latent heat flux temperature tendencies are computed interactively. The RRTMG radiation scheme is used for the computation of shortwave and longwave radiative temperature tendencies. The surface albedo and control insolation are set such that the upwelling and downwelling TOA shortwave radiation match the idealized GCM simulation poleward of 80°. The horizontal atmospheric energy transport induces a temperature structure stable to convection, so including a convection parametrization has no effect. The surface sensible and latent heat fluxes are computed using bulk aerodynamic formulae with 5×10^{-2} drag coefficient and $5\,\text{ms}^{-1}$ near-surface wind speed (Rose, 2018). This SCM is similar to the high-latitude column model in Payne et al. (2015), but instead of parameterizing the atmospheric heat flux convergence and using a fixed distribution of specific humidity, we prescribe them from the idealized GCM. We are unaware of other analyses of SRM that use SCMs, a classic approach in climate science (Manabe & Wetherald, 1967).

Values from the idealized GCM experiments averaged poleward of 80°N are used to prescribe the specific humidity profile, which affects the radiation and surface latent heat flux. In addition, the time-mean advection and condensation temperature tendency profiles from the idealized GCM simulations are added as external temperature tendency terms to simulate the dry and moist components of atmospheric energy transport convergence, respectively. The advective temperature tendency term is calculated in the GCM as the difference in temperature tendency before and after running the dynamics module, and it, therefore, contains both the horizontal and vertical advection temperature tendencies. Because we prescribe atmospheric energy transport to the column model, we consider it to be a "forcing" in this context.

The climatological temperature profiles of the idealized GCM and SCM are similar (Figure S4), though the SCM has an overly strong near-surface temperature inversion compared to the GCM. This may be due to the absence of boundary layer scheme in the SCM, which would smooth differences between the surface and lower atmospheric layers. Similarities between the temperature profiles simulated by the idealized GCM and by the SCM still hold when the latitudinal bounds of the high latitudes is set to 60° (see Figure S5).

We run four simulations: quadrupled CO_2, reduced insolation, perturbed energy transport, and a simulation with all perturbations ($4xCO_2$ and reduced insolation, energy transport, and specific humidity). A summary of the specific parameter settings for each run are given in Table S1. The individual perturbations in the SCM add up to the full response to SRM (Figure S8), which lets us assume that the full response to SRM is composed of a linear superposition of these individual changes.

Figure 2a shows that the idealized GCM's vertical temperature change structure in high latitudes (black, "iGCM") is similar to that of five CMIP5 models in the Arctic (colors, listed in legend). Figure 2b shows the temperature change structure for the different SCM simulations, with points showing surface (or skin) temperature changes. The CO_2-only simulation ("CO_2", red) has a bottom-heavy temperature change structure and a surface temperature increase of 3.1 K. The insolation reduction simulation ("Solar", yellow) has a more vertically uniform cooling structure and a surface temperature change of −1.5 K. The energy transport change ("ET", green) preferentially cools the lower atmosphere and leads to a −0.5 K surface temperature change. Finally, when all perturbations (CO_2, insolation, water vapor, and energy transport) are included ("All", black), the surface temperature change is 1.1 K, as was simulated by the idealized GCM (1.1 K).

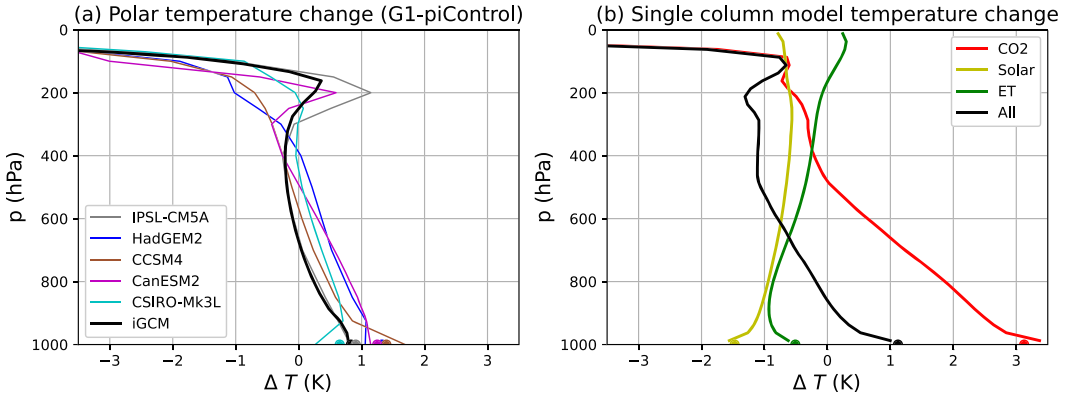

Figure 2. Residual warming arises from bottom-heavy CO_2 warming, while solar forcing and atmospheric energy transport changes have more uniform cooling. (a) Temperature difference between solar geoengineered simulation (G1) and control simulation (piControl) in the Arctic (>80° north) for the idealized GCM (black) and comprehensive GCMs (colors, listed in legend). (b) Decomposition of polar temperature change using the single column model: increased CO_2 (red), reduced insolation (yellow), decreased energy transport (green), and all perturbations (black). The dots at 1,000 hPa show the surface temperature change.

The differences between the comprehensive GCMs (Figure 2a, colors), the idealized GCM (Figure 2a, black), and the SCM (Figure 2b, black) can be due to the different radiation schemes, to the time-averaging of boundary conditions in the SCM, and to the absence of climate components such as clouds, sea ice, and ocean circulation. Our CO_2-only SCM simulation is different from the GCM simulation of Stuecker et al. (2018), where CO_2 forcing is only applied at high latitudes and all other components of the climate system (including energy transport) are free to change. Their diagnosis of the warming contribution from the radiative forcing (their Figure 4) is also different as it separately quantifies the contribution of the lapse rate, whereas the SCM accounts for the vertical structure of temperature change of each component Henry et al. (2020).

We calculate the forcing on the high-latitude atmospheric column for each simulation by calculating the change in outgoing longwave radiation (OLR) induced by the changes in surface and tropospheric temperature (here, the tropopause is set at 200 hPa). The temperature kernel of the column model is calculated by separately increasing the surface and each pressure level by 1 K and calculating the resulting OLR increase (see Figure S7 for kernel structure). The total feedback determines the surface temperature change per unit of forcing and is decomposed into the Planck, lapse rate, and water vapor feedbacks. The change in water vapor is small and induces a negligible change in surface temperature, so it is omitted here (see Figure S8). The Planck feedback is computed as the OLR change from a 1 K temperature increase at the surface and in the troposphere. Its value is $-2.6\,W\,m^{-2}\,K^{-1}$, which is comparable to comprehensive GCM estimates in high latitudes (Feldl & Bordoni, 2016). The temperature feedback is computed as the OLR increase induced by the surface and tropospheric temperature change divided by the surface temperature change, and the lapse rate feedback as the temperature feedback minus the Planck feedback. The lapse rate feedback of the "All" experiment is $1.9\,W\,m^{-2}\,K^{-1}$, which is comparable to the high-latitude lapse rate feedback of the idealized GCM SRM experiment computed using aquaplanet temperature kernels (Feldl et al., 2017) (not shown).

Table 1
Values for ΔT_S, Forcing, and Lapse Rate Feedback for Each Temperature Change Structure of the Single Column Model of the Polar Atmosphere (Figure 2b)

Simulation	ΔT_S (K)	Forcing ($W\,m^{-2}$)	Lapse rate feedback ($W\,m^{-2}\,K^{-1}$)
"4xCO_2"	3.1	5.1	0.79
"Solar"	−1.5	−3.0	0.43
"ET"	−0.51	−1.4	−0.20
"All"	1.1	0.63	1.9

The forcing and lapse rate feedback associated with each simulation are shown in Table 1. There is a $2.1\,W\,m^{-2}$ positive TOA forcing from the difference between the CO_2 and solar forcings and a $-1.4 W\,m^{-2}$ reduction in atmospheric energy transport convergence (comparable to the change in high-latitude convergence of atmospheric energy transport in the idealized GCM). The relatively large surface temperature response in the "All" experiment (1.1 K) for a small forcing ($0.63\,W\,m^{-2}$ if the change in atmospheric energy transport is considered as a forcing on the high-latitude column) can be attributed to the very destabilizing lapse

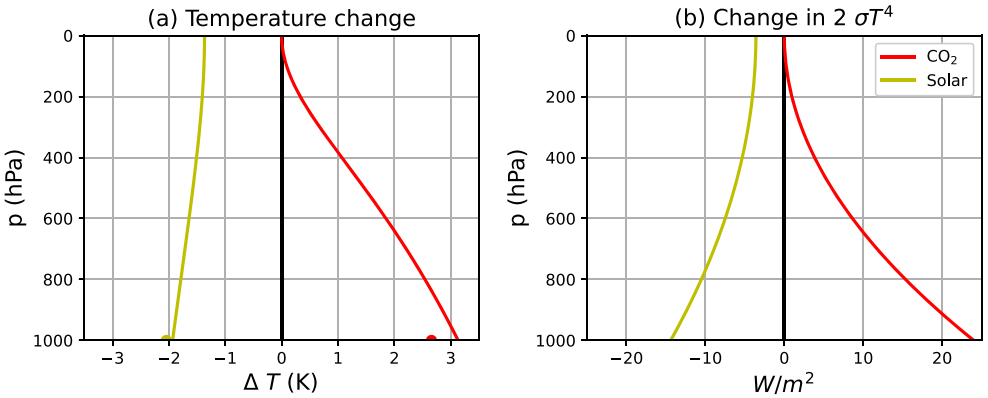

Figure 3. A pure radiative version of an analytical model of the high-latitude atmosphere (Cronin & Jansen, 2016) captures the forcing dependence of lapse rate changes. (a) Temperature change from increasing the total longwave optical depth by 0.2 ("CO_2", red) and from decreasing the surface forcing by 3.6 W m^{-2} ("Solar", yellow), where both forcings are of equal amplitude. The dots at 1,000 hPa show the surface temperature change. (b) Change in $2\sigma T^4$, which satisfies the radiative transfer Equation 3, for both perturbation experiments.

rate feedback (1.9 W m^{-2} K^{-1}). If we use the lapse rate feedback of the CO_2-only simulation (0.79 W m^{-2} K^{-1}), then the surface temperature change would be 0.4 K instead of 1.1 K. We are thus left with explaining this very destabilizing lapse rate feedback that provokes most of the residual polar warming in SRM simulations.

As shown in Figure 2b, the vertical structure of temperature change in the "All" experiment can be decomposed into the effect of individual forcings and feedbacks. The warming from the increase in CO_2 is very bottom-heavy (0.79 W m^{-2} K^{-1} lapse rate feedback), whereas the cooling from changes in insolation and energy transport are more vertically homogeneous. When this vertically homogeneous cooling is superimposed on the bottom-heavy warming from CO_2, it decreases the OLR faster than it decreases the surface temperature. The vertical gradient in temperature is almost left unchanged (compare "CO_2" and "All" in Figure 2b), the forcing on the atmospheric column is small, and the surface temperature change is 1.1 K. Given the importance of the lapse rate changes between forcing agents, we turn to a more idealized SCM to develop a theoretical understanding of forcing dependence of high-latitude lapse rate response.

4. Simplified Analytical Model

The analytical model of the high-latitude atmosphere in radiative-advective equilibrium (Cronin & Jansen, 2016) was used to show the forcing dependence of high-latitude lapse rate changes. In their model, an increase in greenhouse gases leads to a more bottom-heavy temperature change than an increase in atmospheric or surface forcing. Details including the climatological temperature and temperature changes of the analytical radiative-advective model are reproduced from Cronin and Jansen (2016) in Text S1.

The essence of the mechanism for the forcing dependence of the high-latitude lapse rate change is contained in the radiative equilibrium limit (no advection) of the Cronin and Jansen (2016) model, so we discuss this simpler case. We impose the convergence of atmospheric energy transport at the surface to keep the temperatures of this pure radiative equilibrium model similar to high latitudes. The parameters are $F_S = 120$ W m^{-2} and $\tau_0 = 3$, where F_S is the surface forcing and τ_0 the total longwave optical depth. To further simplify the calculations, we do not include an atmospheric window and the optical depth decays as the square of the pressure normalized by the surface pressure.

It is well understood that an atmosphere in pure radiative equilibrium is statically unstable; however, the argument for the perturbation temperature is fundamentally the same as for an atmosphere in radiative-advective equilibrium and easier to understand. In this model, increasing the total longwave optical depth is analogous to increasing atmospheric CO_2, and decreasing the surface forcing is analogous to decreasing the TOA insolation (atmospheric absorption of solar radiation is ignored).

Figure 3a shows the temperature change from increasing the total longwave optical depth (red) and from decreasing the surface forcing (yellow). The total longwave optical depth is increased from 3 to 3.2 and induces an instantaneous reduction in OLR by 3.6 W m^{-2}, which we use for the magnitude of the reduction in surface forcing. The vertical structure of temperature change is more bottom-heavy for an increase in longwave optical depth ("CO_2", red) than for a decrease in surface forcing ("Solar", yellow). The forcing dependence of the lapse rate feedback thus does not depend on the presence of atmospheric energy transport convergence.

To explain this forcing dependence, we derive a simple expression for the temperature structure of the polar troposphere from the two-stream Schwartzchild equations for gray radiative transfer (Equations 1 and 2 in Text S1) with the simplifications described above:

$$2\sigma T(p)^4 = F_S[1+\tau(p)] = F_S\left[1+\tau_0\left(\frac{p}{p_0}\right)^2\right], \tag{3}$$

where F_S is the surface forcing, τ_0 the total longwave optical depth, p the pressure, and p_0 the surface pressure. This equation shows that temperatures must change at all levels for a change in F_S, but they do not change as p goes to zero for a change in τ_0.

Figure 3b shows the difference in $2\sigma T^4$ from changes in τ_0 and F_S. When τ_0 is increased from 3 to 3.2, the change in $2\sigma T^4$ is zero at the TOA and $\delta\tau_0 F_S$ at the surface. When F_S is reduced from 120 W m^{-2} to 116.4 W m^{-2}, the change in $2\sigma T^4$ is δF_S at the TOA and $\delta F_S(1+\tau_0)$ at the surface. Physically, an increase in greenhouse gases corresponds to a deepening of the atmosphere with respect to optical depth and the net upwards longwave radiative flux at the TOA between two equilibrium states is not affected, whereas a change in insolation affects the longwave radiative flux from the surface to the TOA. This reasoning applies for an atmosphere in pure radiative equilibrium, as well as an atmosphere in radiative-advective equilibrium (see Figure S9 for an analog of Figure 3 for an atmosphere in radiative-advective equilibrium).

5. Conclusion

In climate model simulations of SRM scenarios, where the solar constant is reduced to compensate for an increase in CO_2, there is residual warming in polar regions (Figure 1). We decompose the contributions of the CO_2 increase, insolation decrease, and energy transport change to the vertical structure of high-latitude temperature change in order to understand why this residual polar warming occurs. The high latitudes are close to radiative-advective equilibrium: The cooling from radiation is balanced by warming from atmospheric energy transport convergence. Where convection plays a dominant role, the tropospheric temperature change of the atmospheric column is close to independent of the forcing or feedback inducing the temperature change. Without convection, each forcing and feedback induces a different lapse rate response.

In the SRM experiment, the latitudinal structure of the forcing is such that the high latitudes have a positive TOA radiative forcing and a reduction in atmospheric energy transport convergence. If we consider the atmospheric energy transport convergence as a forcing on the high-latitude column, then the positive TOA forcing and reduction in atmospheric transport convergence add up to give a small forcing. However, the surface temperature change is relatively large, which is diagnosed to be a consequence of a destabilizing lapse rate feedback.

The vertical structure of the high-latitude temperature change of an idealized GCM is decomposed using an SCM (Figure 2b). It is shown that the warming from CO_2 alone is very bottom-heavy, whereas the cooling from a reduction in insolation and atmospheric energy transport are more vertically homogeneous. The combination of a bottom-heavy warming and a vertically homogeneous cooling gives a relatively large surface warming despite a small forcing. Using the no advection limit of an analytical model of the high-latitude atmosphere in radiative-advective equilibrium (Cronin & Jansen, 2016), we show that the difference in the vertical structure of temperature changes from increasing CO_2 and decreasing insolation result from different changes in the boundary conditions of the radiative flux (Figure 3). The increase in CO_2 deepens the

atmosphere with respect to optical depth, whereas the change in insolation modifies the resulting longwave radiative fluxes through the whole atmosphere (surface to TOA).

The dominance of the forcing agent dependence of lapse rate changes in provoking residual polar warming in SRM simulations can be assessed by replacing the lapse rate feedback with that of CO_2 (Table 1) or considering models without this feedback (Merlis & Henry, 2018), both of which substantially underestimate the polar warming. An implication of the lapse rate dependence on forcing agent is that there will be residual polar surface warming even if the spatial distribution of scattering aerosols can be optimized to perfectly offset the local TOA greenhouse gas forcing, although not all SRM scenarios have that objective.

Data Availability Statement

Data sets and code for this research are available at https://zenodo.org/record/3711989 (Henry, 2020).

Acknowledgments
This work was supported by Fonds de Recherche du Québec—Nature et Technologies (FRQNT) Nouveau Chercheur award, a Natural Sciences and Research Council (NSERC) Discovery grant, and a Compute Canada allocation. We acknowledge Brian Rose's help in setting up the single-column model by adding an external forcing term.

References

Anderson, J. L., Balaji, V., Broccoli, A. J., Cooke, W. F., Delworth, T. L., Dixon, K. W., et al. (2004). The new GFDL global atmosphere and land model AM2-LM2: Evaluation with prescribed SST simulations. *Journal of Climate*, *17*(24), 4641–4673.

Cronin, T. W., & Jansen, M. F. (2016). Analytic radiative-advective equilibrium as a model for high-latitude climate. *Geophysical Research Letters*, *43*, 449–457. https://doi.org/10.1002/2015GL067172

Feldl, N., & Bordoni, S. (2016). Characterizing the Hadley circulation response through regional climate feedbacks. *Journal of Climate*, *29*(2), 613–622.

Feldl, N., Bordoni, S., & Merlis, T. M. (2017). Coupled high-latitude climate feedbacks and their impact on atmospheric heat transport. *Journal of Climate*, *30*(1), 189–201.

Frierson, D. M. W. (2007). The dynamics of idealized convection schemes and their effect on the zonally averaged tropical circulation. *Journal of the Atmospheric Sciences*, *64*(6), 1959–1976.

Govindasamy, B., & Caldeira, K. (2000). Geoengineering Earth's radiation balance to mitigate CO_2-induced climate change. *Geophysical Research Letters*, *27*, 2141–2144.

Hansen, J., Sato, M., & Ruedy, R. (1997). Radiative forcing and climate response. *Journal of Geophysical Research*, *102*(D6), 6831–6864.

Henry, M. (2019). Polar amplification: What does the temperature feedback have to do with it? (Ph.D. Thesis), Montreal, Canada. https://escholarship.mcgill.ca/concern/theses/ww72bh08q

Henry, M. (2020). matthewjhenry/HM19_SRM: Code and data for Henry and Merlis 2020. Zenodo, https://doi.org/10.5281/zenodo.3711989

Henry, M., & Merlis, T. M. (2019). The role of the nonlinearity of the Stefan-Boltzmann law on the structure of radiatively forced temperature change. *Journal of Climate*, *32*(2), 335–348.

Henry, M., Merlis, T., Lutsko, N., & Rose, B. E. (2020). Decomposing the drivers of polar amplification with a single column model. *Journal of Climate*. https://doi.org/10.31223/osf.io/dzmvq

Huang, Y., Tan, X., & Xia, Y. (2016). Inhomogeneous radiative forcing of homogeneous greenhouse gases. *Journal of Geophysical Research: Atmospheres*, *121*, 2780–2789. https://doi.org/10.1002/2015JD024569

Jucker, M., & Gerber, E. P. (2017). Untangling the annual cycle of the tropical tropopause layer with an idealized moist model. *Journal of Climate*, *30*(18), 7339–7358.

Kalidindi, S., Bala, G., Modak, A., & Caldeira, K. (2015). Modeling of solar radiation management: A comparison of simulations using reduced solar constant and stratospheric sulphate aerosols. *Climate Dynamics*, *44*(9-10), 2909–2925.

Kravitz, B., Robock, A., Boucher, O., Schmidt, H., Taylor, K. E., Stenchikov, G., & Schulz, M. (2011). The Geoengineering Model Intercomparison Project (GeoMIP). *Atmospheric Science Letters*, *12*(2), 162–167.

Laliberté, F., & Kushner, P. J. (2013). Isentropic constraints by midlatitude surface warming on the Arctic midtroposphere. *Geophysical Research Letters*, *40*, 606–611. https://doi.org/10.1029/2012GL054306

Manabe, S., & Wetherald, R. T. (1967). Thermal equilibrium of the atmosphere with a given distribution of relative humidity. *Journal of the Atmospheric Sciences*, *24*(3), 241–259.

Manabe, S., & Wetherald, R. T. (1975). The effects of doubling the CO_2 concentration on the climate of a general circulation model. *Journal of the Atmospheric Sciences*, *32*, 3–15.

Merlis, T. M., & Henry, M. (2018). Simple estimates of polar amplification in moist diffusive energy balance models. *Journal of Climate*, *31*(2018), 5811–5824.

Merlis, T. M., Schneider, T., Bordoni, S., & Eisenman, I. (2013). Hadley circulation response to orbital precession. Part I: Aquaplanets. *Journal of Climate*, *26*, 740–753.

Payne, A. E., Jansen, M. F., & Cronin, T. W. (2015). Conceptual model analysis of the influence of temperature feedbacks on polar amplification. *Geophysical Research Letters*, *42*, 9561–9570. https://doi.org/10.1002/2015GL065889

Pithan, F., & Mauritsen, T. (2014). Arctic amplification dominated by temperature feedbacks in contemporary climate models. *Nature Geoscience*, *7*, 181–184.

Rose, B. E. J. (2018). CLIMLAB: A python toolkit for interactive, process-oriented climate modeling. *Journal of Open Source Software*, *3*(24), 659.

Russotto, R. D., & Ackerman, T. P. (2018). Energy transport, polar amplification, and ITCZ shifts in the GeoMIP G1 ensemble. *Atmospheric Chemistry and Physics*, *18*(3), 2287–2305.

Stocker, T. F., Qin, D., Plattner, G.-K., Tignor, M., Allen, S. K., Boschung, J., et al. (Eds.) (2013). *Climate change 2013: The physical science basis*. Cambridge and New York: Cambridge University Press.

Stuecker, M. F., Bitz, C. M., Armour, K. C., Proistosescu, C., Kang, S. M., Xie, S.-P., et al. (2018). Polar amplification dominated by local forcing and feedbacks. *Nature Climate Change*, *8*(12), 1076.

Xu, K.-M., & Emanuel, K. A. (1989). Is the tropical atmosphere conditionally unstable? *Monthly Weather Review*, *117*(7), 1471–1479.